The Effect of Variable Fuel Staging Transients on Self-Excited Instabilities in a Multiple-Nozzle Combustor

Wyatt Culler[a], Xiaoling Chen[a], Janith Samarasinghe[a], Stephen Peluso[b], Domenic Santavicca[c], Jacqueline O'Connor[d,*]

[a] *Graduate Student, Department of Mechanical and Nuclear Engineering, University Park, PA 16802*
[b] *Assistant Research Professor, Department of Mechanical and Nuclear Engineering, University Park, PA 16802*
[c] *Professor Emeritus, Department of Mechanical and Nuclear Engineering, University Park, PA 16802*
[d] *Assistant Professor, Department of Mechanical and Nuclear Engineering, University Park, PA 16802*

Abstract

Combustion instability in gas turbine engines is often mitigated using fuel staging. Fuel staging, sometimes referred to as fuel splitting, is a strategy by which fuel is unevenly distributed between different nozzles of a multiple-nozzle combustor. These fuel splits are conducted in a transient manner in real engines, and the effects of these transients on instability are not well characterized. This work fills this gap by systematically studying the effects of transient fuel staging on self-excited combustion instability by varying the amount of staging fuel (staging amplitude), timescale in which the fuel is added (transient duration), and whether staging fuel is added or subtracted (transient direction). In this work, three staging amplitudes, five transient durations, and both transient directions are considered. The tran-

*Corresponding author. *Email Address:* jxo22@engr.psu.edu

sient timescales are broadly divided into "short" duration transients, which have fuel delivery timescales shorter than the characteristic instability decay or onset timescales, and "long" duration transients, which have fuel delivery timescales longer than the characteristic instability decay or onset timescales. For short duration transients, we find the instability decay timescale depends on staging amplitude but does not depend on transient duration. For long duration transients, we find the instability decay timescale does not strongly depend on staging amplitude. The instability onset timescale is found to be longer and more variable between runs than the instability decay timescale for a given fuel delivery timescale. The onset timescale is also longer in duration and more variable than the decay timescale at a given fuel delivery timescale, implying that the instability rise process is overall more variable and slower than the instability decay process. Analysis of combustor damping rates show a strong dependence of damping rate on staging amplitude but no strong dependence on transient duration or direction. Instantaneous phase difference images between p' and $\dot{q}'$ are used to differentiate regions in the combustor that have constructive versus destructive interference between heat release rate oscillations and pressure fluctuations. The phase images show that p' and $\dot{q}'$ become in-phase early in the transient for the onset transients.

Keywords: Flame Interaction, Transients, Fuel Staging, Combustion Instability, Gas Turbines

---

1. Introduction

Modern power generation gas turbine engines employ lean, premixed combustion in order to meet NO_X emissions requirements [1, 2]. While running fuel lean successfully reduces NO_X emissions, this strategy often makes the combustor more susceptible to combustion instability. Combustion instability occurs when heat release rate fluctuations and combustor acoustics couple. This coupling drives flow and/or mixture oscillations that further perturb the heat release rate and close the feedback loop. Combustion instability manifests itself as large amplitude pressure fluctuations, which can cause reduced engine operability, increases in NO_X emissions, and, in rare cases, catastrophic hardware failure. The instabilities themselves can couple with different acoustic modes within the combustor, including longitudinal modes, where the acoustic velocity fluctuation is in the axial direction, and transverse modes, where the acoustic velocity fluctuates normal to the mean flow. The focus of this work is longitudinal instabilities.

Combustion instability can be suppressed using passive techniques such as Helmholtz resonators or combustor geometry changes [1], or active techniques such as fuel flow modulation [1, 3, 4]. However, passive techniques are generally preferred in industry for their robustness. Fuel staging is a passive way of suppressing combustion instability in combustors that contain multiple fuel nozzles/injectors. Fuel staging is a strategy by which fuel is un-evenly distributed between different nozzles in a multiple-nozzle combustor. While fuel staging has been shown to effectively suppress combustion instability in industrial hardware [1–3, 5, 6], the mechanism by which fuel staging suppresses longitudinal instability in a multi-nozzle can combustor

has only recently been proposed [7].

A limited number of studies [3, 5, 6] have examined fuel staging as a technique to suppress self-excited instabilities in gas turbine engines. Both Hermann *et al.* [3] and Bulat *et al.* [5] modified the pilot fuel split to suppress instabilities. They showed that the instability could be suppressed and low NO_X emissions maintained with fuel staging, thereby increasing combustor operability. Cohen *et al.* [6] used fuel staging to break the symmetry in an annular combustor in order to suppress transverse instabilities. While these initial studies showed the effectiveness of fuel staging in industrial hardware, they limited the quantification of instabilities to pressure oscillation reduction. The magnitude of pressure oscillation reduction does not provide detailed insight into the flame mechanisms responsible for the instability suppression.

A major effect of fuel staging is the redistribution of fuel, and therefore heat release, in a combustor. Li *et al.* [8] performed a computational study that examined the effect of azimuthally nonuniform heat release rates on longitudinal self-excited instabilities in cylindrical duct with a planar flame. They found that increasing the asymmetry of the heat release rate minimally affected the instability frequency but decreased the instability growth rates. They suggested that the formation of vortical waves, which are only present when the azimuthal distribution of the heat release rates is nonuniform, were at least partially responsible for the stabilizing effect. Although Li *et al.* conducted their study in a simplified geometry, their work suggests that a nonuniform heat release rate distribution has a stabilizing effect on longitudinal instabilities and proposes a physical mechanism as to its success.

Most studies of gas turbine combustion instability have been conducted at "steady" operating conditions, where the mean operating condition (*e.g.* flow rate, equivalence ratio, inlet temperature, etc.) does not change with time; however, there can be significant temporal oscillations about the mean as a result of the instability. While this single-point operation simplifies the analysis and interpretation of measurements, there is increasing interest in the effects of transient operation on gas turbine operability [2], and this concern is only expected to increase as more renewable sources are added to the energy portfolio [2, 9]. Significantly fewer studies of combustion instability have been conducted where the operating point is varied during the test. The limited literature on these transient studies can be broadly classified into triggering studies [10], stability transition studies [3–6, 11–16], intermittency studies [11, 17], and hysteresis studies [11, 18, 19].

Of all of the literature on transient operation, stability transitions studies appear to be the most numerous [3–6, 11–16]. These instability transition studies can be further subdivided into two categories: those that use active control to prompt instability transitions [4, 13, 14] and those that examine spontaneous transitions during steady or quasi-steady operation [11, 12, 15, 20]. Early work by Poinsot *et al.* [4] used active instability control from a loudspeaker on the fuel line in order to break the thermoacoustic feedback loop in a non-premixed combustor undergoing self-excited instabilities. Breaking the feedback loop allowed them to investigate the instability growth rates in the combustor. They noted hysteresis in the stability transition; higher amplitude acoustic excitation was required to damp the instability than was required to prevent the stable combustor from be-

coming unstable. Recent work by Noiray and Denisov [14] used a similar active control method to validate a method to extract the linear growth rate during the transition from stable to unstable and noted the stochastic nature of the transition.

Spontaneous stability changes happen at bifurcation points, when the the combustor is operated at the limit of the stability margin, or when there is significant intermittency in the instability amplitude. Kabiraj and Sujith [11] used a confined, conical flame burner to study spontaneous changes in system stability by varying the flame location in a quasi-steady manner. They noted that the combustor could undergo quasi-periodic oscillations, limit cycle oscillations, or intermittent amplitude oscillations depending on both the flame location and the direction of the change. This hysteretic behavior was attributed to a subcritical Hopf bifurcation. Their work highlights the importance of direction on the end state (periodic limit cycle, quasi-periodic limit cycle, etc.), as well as the hysteresis that can occur at the transition point. Kheirkhah *et al.* [15] recently studied spontaneous stability transitions in a high pressure, liquid-fueled combustor. They used a novel image processing technique to analyze the instantaneous phase relationships between pressure and heat release rate to study the regions of the combustor that contributed to the instability. Using statistics conditioned on whether the instability amplitude was rising or falling, they were able to identify some of the mechanisms that might drive changes in instability amplitude. Boxx *et al.* [16, 20] recently studied spontaneous instability transitions in a high pressure, swirl-stabilized combustor at a bi-stable operating point. They found that the spontaneous transition to instability was caused by a gradual

accumulation of hot gases in the outer recirculation zone that destabilized the outer shear layer. Analysis of the combustor pressure fluctuations with wavelet transforms also showed that the instability onset was preceded by a shift in the peak frequencies of the combustor, suggesting a possible precursor to instability.

While the current literature provides some insight into the behavior of combustion systems during transients, this is a relatively new, yet important, area of study that warrants careful treatment. Most of the transient studies conducted thus far have focused on the beginning or end states of the transition. While this serves as an important foundation for understanding the long-time limit effects of transients, it is also important to understand the processes along the instability transition path, as these may have an effect on the end state. Furthermore, the studies that considered the transient path [4, 14, 15, 20] focused on spontaneous instability transitions at a single operating condition. While these studies provide important insight into the transient process, they only address transients in a certain context. The present work addresses transient operation in a fundamentally different context than the previous work. In particular, we command the transient in a controlled manner by using a defined, quantifiable transient "input" and measure the system response to that input. In the present experiment, the transient input is the quantity of additional staging fuel varied in the center nozzle of the four-around-one multi-nozzle combustor, and it is controlled with a proportional-control valve that can regulate the amount of fuel and rate at which fuel is delivered to the system. This fuel-staging rate is quantified through the use of IR absorption measurements, thereby allowing us

to define the "input" transient to the system. The transient response of the system is characterized using a combination of combustor pressure data and high-speed CH* chemiluminescence images.

In this study, a transient is defined using three quantification metrics—the transient *duration*, *direction*, and *amplitude*. The *duration* is the time over which the transient input is executed. The *direction* is the direction of fuel modulation (e.g., fuel flow increases vs. decreases), and the *amplitude* is the absolute difference in fuel flow from the beginning to the end of the transient. This systematic investigation is not possible in spontaneous transition studies, and this methodology allows us to understand the sensitivity of system response to different timescales of transient operation and collect data over a larger number of ensembles. For example, consider an input transient that is commanded as an "impulse," or a change in fuel flow at a timescales shorter than other timescales in the system (e.g., convection, recirculation, and heat transfer). After the impulse input, the system may transition from one state to the next in a very different way than if the input transient timescale was very slow, allowing for long-timescale processes like heat transfer to equilibrate over the course of the transient. In this work, we use these variations in "transient path" to elucidate key physical processes in the onset and decay of combustion instabilities.

2. Experimental Setup and Diagnostics

Experiments are conducted in a multi-nozzle can combustor, described in detail by Samarasinghe *et al.* [21] and shown in Fig. 1. Five nominally identical, industrial scale, swirl, and bluff body stabilized nozzles are arranged

in a "four-around-one" configuration. To provide optical access of the flame, the combustor liner is a 260 mm diameter, 300 mm long quartz tube that is open ended (thus combustion occurs at atmospheric pressure). This combustor burns a fully premixed mixture of preheated air and natural gas. The experimental parameters are contained in Table 1.

Table 1: Summary of Experimental Conditions

Parameter	Value
Inlet Temperature	200 C
Nozzle Bulk Velocity	26 m/s
Inlet Reynolds Number (Re_D)	17,000
Nozzle Swirl Number	0.7
Air Mass Flow Rate	0.142 kg/s
Thermal Power	65 kW

2.1. Fuel Staging

Fuel staging is accomplished by injecting a small amount of additional fuel into the center nozzle, as shown by the schematic in Fig. 2. This fuel injection causes a similar (but not equal) decrease in the fuel flow rate of the outer nozzles. The net result of fuel staging is a slight increase in global equivalence that is no more than 3% of the total fuel flow during staging; the primary effect of fuel staging in this combustor is to redistribute the heat release rather than increase the thermal power. Uniform increases in equivalence ratio in all nozzles at this operating condition result in self-excited instabilities, therefore it is the fuel staging and not the equivalence

ratio change that is suppressing the instability [7]. Each fuel nozzle consists of an annulus, a swirler, and a centerbody, as shown by the schematic in Fig. 2. Premixed fuel and air flow through the annulus of the nozzle (blue path), while staging fuel is injected below the swirler in an internal fuel circuit (red path). The staging fuel enters the premixed mixture through small holes in the swirler, and the combined mixture (purple section) then flows to the flame. While the staging fuel is injected about 7 hydraulic diameters before the flame, previous measurements [22] indicate the fuel is well mixed at the nozzle exit. Additionally, the amount of staging fuel diverted through the swirler represents a small fraction (less than 5%) of the overall fuel flow rate. The fuel delivery profile and convective delay depends on both the staging amount and staging direction, and is measured using an infrared absorption technique at equivalent non-reacting conditions as described in the supplementary material and summarized in Table 2. The equivalence ratio of the center nozzle with the additional fuel injection is termed the "staging equivalence ratio" and symbolized by $\phi_{Staging}$.

The fuel delivery is controlled by a Humphrey PC3 proportional control solenoid valve, which is located approximately 12 inches (30 cm) upstream of the staging fuel injection location shown in Fig. 2. The solenoid valve is controlled using a National Instruments DAQ system. The valve is commanded to open or close using a linear ramp, where the transient duration, $\tau_{Transient}$, is defined as the duration of the control signal ramp. The relationship between commanded duration and fuel delivery timescale is shown in Table 2.

2.2. Experimental Diagnostics

The heat release rate fluctuations from the flame are visualized using CH* chemiluminescence measurements, a widely used technique in hydrocarbon-air premixed flames [23, 24]. High-speed CH* chemiluminescence images are obtained using a Photron SA-4 high speed camera fitted with an Invisible Vision UVi 1850-10 intensifier, a Nikon AF Micro-Nikkor 60mm f/2.8 lens, and a 432 nm $\pm$ 5 nm bandpass filter. The spatial resolution is 0.5 mm/pixel, and each image has a size of 640 by 624 pixels. Images are captured at 4000 frames per second for either one or four seconds, depending on the test. Dump plate pressure (PCB 112A22) and global photomultiplier tube (Hamamatsu H7732-10) measurements of CH* chemiluminescence are taken for 8 seconds for short-duration transients and 16 seconds for long-duration transients at a sampling rate of 16,384 Hz; this data acquisition results in a frequency resolution of 0.125 Hz. All pressure data are high-pass filtered in the frequency domain (discarding frequencies below 10 Hz) before further processing is conducted. The dominant instability frequency in this work is approximately 530 Hz, which is the quarter wave mode of the combustor. The wavelength of the acoustic wave, 1.2 m, is much longer than the flame. Therefore, the pressure is considered to be uniform along the flame length and equivalent to the pressure measured at the dump plane.

Two transient directions are considered in this work: instability decay and instability onset. Examples of the transitions are shown in Figs. 3*a* and 3*b*, respectively. The bottom half of each figure shows the combustor pressure time trace in blue and the envelope of the pressure in red, and the top half shows the power spectral densities before and after the transient. Self-excited

instabilities exist when all nozzles are fueled equally at an equivalence ratio of $\phi = 0.70$, as shown by the pressure trace at the beginning of the decay transient in Fig. 3*a* or the end of the instability onset transient in Fig. 3*b*. The instability is suppressed when the center nozzle equivalence ratio is increased, as shown by the pressure traces at the end of the decay transient in Fig. 3*a* or the beginning of the onset transient in Fig. 3*b*. The time when the instability is suppressed by fuel staging is termed the staged-stable region; this is highlighted in Fig. 4. While the global equivalence ratio changes slightly during the transient, the primary effect of fuel staging is to change the distribution of heat release. The steady-state stability map at this operating condition is discussed in Ref. [7].

The 1 ms transient duration, the shortest of all tested durations, is also termed the "impulse" transient. We use this impulse transient to characterize the natural timescales of the system, as the system responds to impulse inputs at its natural, characteristic timescales. Two classes of transient durations are considered: "short" transients and "long" transients. The 1 ms, 16 ms, and 58 ms are "short" duration transients because these transients timescales are shorter than or on the order of the natural timescales obtained for the impulse transients. The "long" duration transients are thousands of milliseconds, which is much longer than the natural timescales. The convective timescale based on flame length is approximately 3.8 ms and the acoustic timescale for an instability at 530 Hz is 1.8 ms.

The fuel delivery profile is measured using an infrared absorption technique conducted at equivalent non-reacting conditions; plots and additional details are described in the supplementary material. The spatial fuel delivery

Table 2: Test Matrix

$\tau_{Transient}$ (ms)	$\phi_{Staging}$	$\tau_{Fuel,Decay}$ (ms)	$\tau_{Fuel,Onset}$ (ms)
1	0.75	33	20
	0.80	20	13
	0.85	15	9
16	0.80	23	14
	0.85	19	10
58	0.80	21	14
	0.85	17	11
4,000	0.80	108	496
	0.85	230	645
10,000	0.80	413	876
	0.85	707	1026

time, τ_{Fuel}, differs from $\tau_{Transient}$ due to convective delays in the fuel lines. The characteristic delivery timescale, τ_{Fuel}, is obtained by fitting a logistic equation of the same form as Eq. 1 to the fuel concentration signal, and calculating the characteristic time using Eq. 2.

2.3. Data Screening

A small fraction of outlier cases do not transition from an unstable condition to a stable condition or vice-versa. The focus of the present work is to examine the stability transition process; therefore, we limit our analysis to cases that transition from a strongly unstable condition to a stable condition or vice-versa. Two separate criteria must be met in order for a condition to

be considered unstable. First, each case must have a sufficiently large instability amplitude, and second, each case must have a sufficiently narrowband frequency peak. To be considered a sufficiently strong amplitude instability, the combustor pressure RMS fluctuation must be greater than 0.07 PSI (0.483 kPa), which is 0.5% of the mean combustor pressure. The combustor pressure must additionally have a peak power spectral density amplitude 30 times greater than the average amplitude of all other frequencies. These screening criteria remove 13% of the 192 decay cases and 7% of the 167 onset cases collected for this work.

3. Data Analysis Methods

3.1. Characteristic Time Calculation

The combustor pressure time trace is used to characterize the instability amplitude, the staged-stable amplitude, and the timescale of the transition. The instability amplitude and the staged-stable amplitude are obtained from the RMS of the pressure fluctuations before or after the transition. The timescale of the transition is obtained by fitting the logistic curve in Eq. 1 to the envelope of the pressure, then measuring the width of the curve using Eq. 2. The envelope itself is obtained by taking the magnitude of the analytic signal, which is obtained using the Hilbert Transform. This approach has been used by others [15, 25] to obtain the envelope of a sinusoidal pressure time series.

$$p'(t) = \frac{A - B}{1 + e^{k(t-t_0)}} + B \tag{1}$$

In Eq. 1, A is the limit cycle amplitude, B the staged-stable amplitude, t_0 the curve center, and k, the exponential decay factor. The model is symmetric relative to t_0. This sigmoid curve captures the dual-asymptote behavior of a combustor transitioning from stable to unstable operation or vice-versa, and allows an unambiguous characteristic time to be defined based on the width of the curve. The characteristic time given by Eq. 2 represents the time it takes for the instability amplitude to rise or decay to $\frac{A-B}{e}$.

$$\tau = |\frac{ln(2e-1)}{k}| \tag{2}$$

Figure 4 shows a graphical illustration of the logistic model applied to (a) instability decay and (b) instability onset. The pressure time series is shown in blue and the model fit is shown by the black dotted line (color online). The black lines show the extent of τ, the characteristic decay (or onset) time. The model is fit to the data using a least-squares nonlinear regression. In all cases, the model is fit to the data for 4 seconds, or approximately 65,000 data points. The fit parameters are not found to be strongly dependent of the start time of the fit nor the initial parameter guesses as long as the algorithm converges. However, to reduce any statistical bias, the start time for the fit is adjusted on a case-by-case basis to ensure the instability transition happens near the middle of the fit time.

3.2. Combustor Damping Rate Calculation

The net combustor damping rate is calculated using the approach described by Stadlmaier *et al.* [26], which is based on the method proposed by Lieuwen [27]. Reference [28] contains a summary of other approaches.

The equation for combustor pressure follows the treatment by Culick [29], where it is assumed the acoustic pressure inside of a combustor is due to the superposition of I nonlinearly interacting harmonic oscillators [26, 27, 29]. The superposition of these oscillators is represented by a second order system written in Eq. 3 [26].

$$\sum_{i=1}^{I} \ddot{\eta}_i + 2\nu_i\dot{\eta}_i + \omega_i^2\eta_i = \zeta(t) \tag{3}$$

In this equation, i is the current mode, η_i the current modal amplitude, ν_i the net damping rate, ω_i the angular frequency, and finally $\eta(t)$ the stochastic driving. Using Eq. 3, it can be shown that the autocorrelation of the pressure is related to the total damping rate, including both thermoacoustic and acoustic damping, as shown in Eq. 4 [26].

$$ACF(\tau_{Lag}) = \sum_{i=1}^{I} exp(-\nu_i\tau)cos(\omega_i\tau_{Lag}) \tag{4}$$

In this equation, ACF is the autocorrelation function, and τ_{Lag} is the current autocorrelation lag of the pressure fluctuation. The right hand side of Eq. 4 is fit to the autocorrelation of the pressure fluctuation in the time domain in order to extract the damping rate. Baynesian network modeling, which uses Markov Chain Monte Carlo methods to simulate probability densities of the different fit parameters, is a robust way of fitting. The software package JAGS [30] is used for fitting. The net damping rate is extracted by fitting Eq. 4 to a 1 second autocorrelation of the pressure during the staged-stable portion of the transient as shown in Fig. 4. A fit length of 10 autocorrelation cycles was chosen based on the results of a sensitivity study using synthetic data; this fit length results in less than 10 percent error for

the damping rates and instability frequencies encountered in this combustor. The error in frequency estimation was less than 1 percent at all damping rates. While this work focuses on comparing damping rates, others [14, 31] describe methods to calculate growth rates as well.

3.3. Instantaneous Phase Difference Images

The Rayleigh index, as shown in Eq. 5, is a common metric used to characterize the propensity of combustion systems to undergo instability. In this equation, T is the period of an acoustic oscillation, Ω the flame integration volume, $p'(\vec{x},t)$ the combustor pressure as a function of time and space, and $\dot{q}'(\vec{x},t)$ the heat-release rate as a function of time and space. When the Rayleigh index is positive, energy is added to the acoustic field, and when the Rayleigh index is negative, energy is removed from the acoustic field. Instability occurs when the Rayleigh index is positive and the energy added to the acoustic field is greater than the energy lost due to damping, radiation, or convection. The disadvantage with using the Rayleigh index is that it requires accurate measurements of the relative heat release rates, which are not always possible when the equivalence ratio is nonuniform. However, the sign of the Rayleigh index is determined by the relative phase difference between $p'(\vec{x},t)$ and $\dot{q}(\vec{x},t)'$, which is not sensitive to local variations in equivalence ratio [15]. The instantaneous phase between these two quantities is obtained using the Hilbert transform.

$$RI(T) = \int_0^T \int_\Omega p'(\vec{x},t)\dot{q}'(\vec{x},t)d\Omega dt \tag{5}$$

A $\pm$25 Hz bandpass filter centered about the peak instability frequency is applied to both the pressure time series and image data before the instanta-

neous phase is calculated. In the case of the images, each pixel is considered to be an independent time series. The filtering process is as follows: first, each time series is converted to the frequency domain. Next, all frequency coefficients outside of the bandpass window are zeroed. Finally, the data is converted back to the time domain before subsequent processing. This method of filtering does not introduce a phase delay. Each pixel of the filtered image is averaged into a 2x2 "superpixel," then the Hilbert transform is taken of the time series of that superpixel. The instantaneous phase is calculated by taking the angle between the real and imaginary components of the Hilbert transformed time series and subtracting the instantaneous phase of the pressure data at the same time. This method has recently been used by Kheirkhah *et al.* [15] to examine instability in a liquid fueled, high pressure combustor.

4. Pressure Amplitude and Timescale Analysis

4.1. p'_{RMS} Before and After The Transient

The fuel staging effectiveness, quantified by the reduction in combustor pressure amplitude, is assessed by comparing the p'_{RMS} amplitudes before and after the transient. The p'_{RMS} amplitude is calculated using one second of pressure data both before and after the transient. For cases with a staging amplitude greater than $\phi_{Staging} = 0.75$, the before and after transient regions defined as the "staged-stable" regions are shown in Fig. 4. For the $\phi_{Staging} = 0.75$ cases where a logistic fit was not always possible, a two second offset from the valve actuation was chosen for the averaging region. These offsets ensure the change in pressure amplitude during the stability transition does

not skew the p'_{RMS} amplitudes of the end states.

Fig. 5 summarizes the p'_{RMS} amplitudes as boxplots. The y-axis shows the combustor pressure fluctuations in kPa,the x-axis shows the staging amplitude, and the arrows link the initial amplitude to the final amplitude. In this and all subsequent boxplots, D denotes decay transients, O denotes onset transient, U denotes un-staged conditions and S denote staged conditions. The upward and downward facing triangles depict the 95% confidence interval on the median [32]. The inner quartile range (IQR), a robust measure of spread of the data [33], is given by the distance between the top (third quartile) and the bottom (first quartile) of the box. Outliers, which are conventionally defined as 1.5 times the inner quartile range, are plotted as red crosses. The vertical dotted lines are the boxplot "whiskers" and extend to whichever is shorter: the minimum/maximum of the data set or 1.5 times the inner quartile range in the case where there are outliers. The horizontal, dotted line shows the cutoff between stable and unstable p'_{RMS} amplitude (defined as 0.5% of atmospheric pressure). Finally, the numbers at the top of each boxplot indicate the number of ensembles for each test. The other transient durations show the same trends and are omitted for brevity.

Figure 5 shows that the $\phi_{Staging} = 0.75$ staging amplitude does not reliably suppress the instability, as the median staged p'_{RMS} amplitude is unstable both before and after staging. In contrast, the other staging amplitudes show a clear stability transition as the staged portions are universally stable, and the un-staged portions universally unstable. Failure of $\phi_{Staging} = 0.75$ staging to suppress instability indicates there is a minimum effective staging amplitude. Section 4.2.2 examines this minimum staging amplitude,

termed the bifurcation equivalence ratio, where it is found to be approximately $\phi_{Staging} = 0.76$. Additionally, when the combustor is unstable, the inner quartile range is much larger than it is when it staged stable. This also true on a percentage basis, where the unstable IQR is about 30% of the median pressure fluctuation amplitude and the stable IQR is about 10% to 15% of the median pressure fluctuation amplitude. This indicates the unstable RMS amplitudes are more variable than the stable RMS amplitudes in both an absolute and relative sense. Finally, the boxplots indicate the median un-staged, unstable p'_{RMS} amplitudes are not statistically significantly different from each other across staging amplitudes, indicating that the instability amplitude of the combustor is repeatable across many tests.

4.2. Characteristic Time Analysis

The previous section analyzed the end states of the transients by considering the RMS amplitude of the combustor pressure. This section analyzes the transition timescales for short and long duration transients. For brevity, the discussion is limited to the $\phi_{Staging} = 0.85$ amplitude, as the trends for the $\phi_{Staging} = 0.80$ cases are similar.

4.2.1. Short Duration Transients

Figure 6 shows boxplots of the characteristic decay timescale, calculated using Eq. 2. The y-axis shows the characteristic decay time, in milliseconds. Figure 6 shows that there is not a statistically significant difference in decay timescale between different short transient durations, as the confidence intervals overlap. This result implies that all the short duration decay transients behave similarly to the impulse transients, and this similarity in decay

timescales for short duration transients is consistent with the similarity in fuel timescales in Table 2. However, the median instability decay timescale is longer than the median fuel delivery timescale, indicating that the instability decay depends on processes other than fuel convection. In other words, the time-varying equivalence ratio, $\phi(t)$, for these short timescale transients is not quasi-steady with regards to the instability decay.

Figure 7 shows a boxplot summary of characteristic onset times calculated using Eq. 2 for the short transients. Figure 7 shows that the characteristic instability onset time for short-duration transients does not depend on transient duration nor staging amplitude, as all estimated confidence intervals on the median overlap. This suggests that the instability onset process is largely independent of the initial condition. Additionally, at a given transient duration and staging amplitude, the characteristic onset timescales in Fig. 7 are much longer than the decay times at the same amplitudes and timescales in Fig. 6 and the fuel convective timescales in Table 2. This comparison indicates that the fuel delivery process is not quasi-steady relative to the instability onset process, as the onset process is much longer. The IQR for the instability onset is also much larger than the IQR for the instability decay. The increased IQR indicates that the processes controlling the instability onset have longer timescales, significantly more intermittency, or both, than the processes that control the instability decay. Finally, the increased variability in the onset time scales are not due to increased variability in the fuel delivery timescales, as Figure 4 in the supplementary materials shows the fuel delivery timescale for short transients does not have a statistically significant dependence on direction. The reasons for the increased intermittency

during instability onset are the subject of current research.

4.2.2. Long Duration Transients

Figure 8 shows the characteristic decay times as a function of staging amplitude for $\tau_{Transient} = 4000ms$ and $\tau_{Transient} = 10000ms$. The trends follow for $\phi_{Staging} = 0.80$. Figure 8 indicates that decay times depend on $\tau_{Transient}$, where longer transients have longer decay τ. This dependence on commanded duration suggests that the change in equivalence ratio during the long duration transients is slow enough that the mechanism responsible for the stability transition can "keep up" with the changing equivalence ratio. As such, the time-varying equivalence ratio, $\phi(t)$, for the long duration transients appears quasi-steady-state relative to the instability decay processes. While τ for the long duration decay times in Fig. 8 are longer than τ for short duration decay in Fig. 8, the long duration transient τ is still significantly shorter than $\tau_{Transient}$. This rapid transition suggests there is a critical bifurcation equivalence ratio, beyond which the combustor rapidly becomes stable.

Figure 9 shows boxplots of τ for the $\tau_{Transient} = 4000ms$ and $\tau_{Transient} = 10000ms$ onset transients. The y-axis range has been truncated to highlight the difference between boxplot quartiles; this truncation obscures one outlier at 2593 ms for the $\phi_{Staging} = 0.85$ onset case. Unlike τ for the long duration decay transients, the long duration onset transient τ does not show a strong dependence on $\tau_{Transient}$. As mentioned previously, τ for the long duration onset transients is still much shorter than $\tau_{Transient}$.

The characteristic time analysis shows for both short and long $\tau_{Transient}$ the instability onset process is longer and more variable than the instability decay process, and additionally does not have a strong dependence on initial

staging amplitude. However, it is interesting that both transient regimes show similar behavior given that τ_{Fuel} is shorter than τ for short duration transients but the opposite for long duration transients.

The bifurcation equivalence ratio, $\phi_{Staging}(t_0)$, is defined as the equivalence ratio at t_0. The parameter t_0 measures the halfway point between pressure asymptotes, and is therefore both an unambiguous and physically meaningful measure of the equivalence ratio at the stability transition. Figure 10 illustrates how the bifurcation equivalence ratio is calculated. The blue trace (color online) in Fig. 11 shows the combustor pressure, the black trace shows the logistic fit to the combustor pressure, and the red line shows the calibrated equivalence ratio, as obtained from the infrared absorption measurements. The bifurcation equivalence ratio is shown by the intersection of the green lines with the red $\phi(t)$ line. We expect the equivalence ratio at t_0 to be independent of valve timescale provided the change in equivalence ratio is quasi-steady relative to the change in pressure.

Boxplots of $\phi_{Staging}(t_0)$ are shown in Fig. 11. The y-axis shows the staging equivalence ratio at t_0, while the x-axis shows the staging amplitude. Figure 11 illustrates that the median value for each staging amplitude at each timescale is roughly centered within the inner quartile range, indicating that the distributions are symmetric. Figure 11 also shows the median equivalence ratio at t_0 is between $\phi_{Staging} = 0.74$ and $\phi_{Staging} = 0.79$ for all test cases, with the most common transition at $\phi_{Staging} = 0.75$. The fact that the transition generally occurs near $\phi_{Staging} = 0.75$ suggests that the reason the $\phi_{Staging} = 0.75$ cases have large variability in the pressure amplitudes and rarely stabilize the combustor is that they are on the stability margin.

Figure 11 additionally shows that the median transition equivalence ratio does not generally have a strong dependence on direction, suggesting there is no hysteresis when the change in equivalence ratio is quasi-steady relative to the instability transition timescale. It is unclear why the bifurcation equivalence ratio for $\phi_{Staging} = 0.85, \tau_{Transient} = 4000ms$ significantly differs from the other $\phi_{Staging} = 0.85$ bifurcation equivalence ratios. It may be that $\phi(t)$ is not quasi-steady relative to the transition process for the onset case, as the distribution of onset times in Fig. 9 shows many onset cases have timescales about the same order as τ_{Fuel} shown in Table 2. More discussion of the bifurcation equivalence ratio can be found in Ref. [34]

5. Combustor Damping Rates

The combustor damping rates are used to quantify the stability margins of the combustor by determining the amount of damping. A system with larger overall damping has a larger stability margin than a system with less damping. The effect of damping is to de-correlate fluctuations at one time with fluctuations at a previous time, and the fluctuations in a system with larger damping will de-correlate in less time than one with smaller damping. The correlation time is inversely proportional to *damping rate*, and this proportionality shows how damping rates can be related to overall damping. Figure 12 shows the autocorrelation of the pressure and the resultant JAGS fit for the median impulse decay transients at $\phi_{Staging} = 0.80$ in Fig. 12a and $\phi_{Staging} = 0.85$ in Fig. 12b. The combustor pressure fluctuation during the one second of test data is shown by the trace at the top of each figure, which is taken during the staged-stable portion of the transient, as shown in Fig.

4. The autocorrelation of the combustor pressure fluctuation is shown at the bottom of each figure, while the resulting autocorrelation fit is shown in a lighter color on top. The net damping rate and the instability frequency is shown at the bottom right of each figure. While the differences in pressure fluctuation time traces are more subtle in Figs. 12a and 12b, it is clear from the autocorrelation fit that the damping rate for $\phi_{Staging} = 0.80$ is significantly less than the damping rate for $\phi_{Staging} = 0.85$. This indicates that the higher staging amplitude results in a more stable combustor. Figure 12 also highlights the utility of using the damping rate as a comparison metric; the differences in damping rates are larger than the differences in staged-stable p'_{RMS} amplitudes.

Damping rate distributions are summarized using boxplots in Fig. 13, which show the staging equivalence ratio and direction on the x-axis, the damping rate on the y axis, and the transient duration above. Figure 13 indicates that at all timescales, larger staging amplitudes result in larger damping rates. These differences are significant as the medians do not overlap. However, the damping rates do not show a strong sensitivity to timescale or direction for all investigated timescales 4,000 ms or less, as the confidence intervals overlap. However, the 10,000 ms transients show a systematically lower damping rate than given equivalence ratio than the other timescales. A possible reason for this difference in damping rates is the wall temperature at the flame stabilization point. The combustor has more time to heat up over the course of a long-duration transient than it does for a short-duration transient, and this difference in temperature may cause a decrease in damping rates for the long duration transients.

Additionally, the damping rate for $\phi_{Staging} = 0.85$ is roughly two times the damping rate for $\phi_{Staging} = 0.80$ at a given transient duration. The difference in median decay τ between $\phi_{Staging} = 0.85$ and $\phi_{Staging} = 0.80$ is also about a factor of two (note the distributions of $\phi_{Staging} = 0.80$ have been omitted for brevity), suggesting the decay times for short transients are related to the asymptotic damping rates. This also implies that the change in damping is significantly faster than the instability decay. While the long duration transients show between a factor of two and three difference in damping rates between the staging amplitudes, the decay timescales for each staging amplitude do not show as clear of a trend. This is likely due to the fact the damping changes more gradually during the long duration transients, and this gradual, perhaps stochastic, change in damping during the long duration transients causes a less clear trend in the decay timescale. Analysis of the reconstructed phase space, using the method described in the supplementary material, supports this conclusion. Animations of the phase space reconstructions for both long and short duration transients at $\phi_{staging} = 0.85$ are shown in the supplemental materials, and show discrete changes in the attractor diameter during the transient.

6. Instantaneous Phase Analysis

Images of the instantaneous phase difference between the combustor pressure fluctuations and the heat release rate, where heat release rate is estimated using CH* chemiluminescence, provide temporally- and spatially-resolved data that identify the regions of the combustor that have constructive or destructive interference. As noted by Kheirkhah *et al.* [15], the

instantaneous phase is not sensitive to variations in CH* intensity caused by local equivalence ratio variations, and can be applied in cases where the equivalence ratio is nonuniform. The flame structure is captured by the time-averaged CH* chemiluminescence image in Fig. 14*a*. The CH* intensity is used as a qualitative marker of heat release rate; regions that are dark (lower CH* intensity) have lower heat release rates than regions that are bright (higher CH* intensity). The rectangles at the bottom of Fig. 14*a* show the left nozzle (L), the center nozzle (c), and the right nozzle (R). Figure 14*a* indicates the largest region of heat release rate occurs in the center of the combustor; this high heat release rate is caused by a combination of flame interaction effects [35] and the line-of-sight integration over three flames in this view. Figure 14*b* shows the instantaneous, absolute phase difference of $|\Phi(p') - \Phi(\dot{q}')|$. Note that while both Fig. 14*a* and Fig. 14*b* use the same colormap, the units of Fig. 14*a* are arbitrary intensity, while the units of Fig. 14*b* are absolute phase difference in radians. In Fig. 14*b*, light regions are regions that have destructive interference, while dark regions are regions that have constructive interference between the pressure and heat release rate. The white line shows the $\pi/2$ isocontour that delineates driving from damping. The center of the combustor is dark in Fig. 14*b*, indicating there is net acoustic driving by the flame in this instant. The largest heat release also occurs in this region, indicating this is high amplitude acoustic driving. The center combustor region is emphasized in the subsequent discussion due to the large concentration of heat release there.

6.1. Short Duration Transients

Figure 15 shows snapshots of instantaneous phase for the median $\phi_{Staging} = 0.85, \tau_{Transient} = 1ms$ decay transient. The focus is restricted to $\phi_{Staging} = 0.85$, as the other staging equivalence ratios for short duration transients show similar trends. Each image in Figs. 15-16 show snapshots of $|\Phi(p') - \Phi(\dot{q}')|$. The corresponding pressure time trace is at the bottom of each figure, where vertical lines show the time of each instantaneous phase snapshot. It should be cautioned that these instantaneous phase images are line-of-sight integrated, and at this viewing angle, the imaging integrates over the center flame and two of the outer flames, as indicated in 14*a*.

Figure 15*(a)*, taken well before the start of the transient, shows there is strong constructive interference between the pressure and heat release in the center of the combustor. This is also the region of highest heat release rate. Figure 15*(b)*, taken at the start of the pressure decay, shows the growth of an out-of-phase region in the center of the combustor. These bright structures grow in size as the transient progresses to the halfway point at t_0, as shown in Figure 15*(c)*, and by Fig. 15*(d)* the bright, out-of-phase region has displaced much of the dark, in-phase region that formerly dominated the center of the combustor. The bright, out-of-phase structure persists even to 3τ after the center of the transient, as shown in Fig. 15*(f)*, despite low pressure amplitudes. The persistence of structure suggests that a phase cancellation effect between the center flame and the outer flames is responsible for the suppression of the longitudinal instabilities in this combustor; this point is further supported in work by Samarasinghe *et al.* [7]. However, it is interesting to note that the flame bases remain out-of-phase for the duration of

the transient, suggesting that the flame base does not tend to contribute to the instability. Due to the line-of-sight nature of CH* chemiluminescence, it is difficult to say with absolute certainty whether this out-of-phase region is due to changes in the center flame, change in flame interaction, or some combination of the two. However, we suspect that this change is likely due to a change in the flame length of the center flame which then changes the interaction dynamics. This observation is based on OH planar laser induced fluorescence imaging done in a previous study by Samarasinghe *et al.* [7].

Figure 16 shows a representative $\phi_{Staging} = 0.85, \tau_{Transient} = 1ms$ onset transient. Well before the transient in Fig. 16*(a)*, fluctuations in the center of the combustor is are out-of-phase, resembling the end state of the decay transient in Fig. 15*(f)*. Much of the center region of the combustor is already in-phase by the start of the pressure rise Fig.16*(b)*, though the flame base stays out-of-phase similarly to the decay transient. The structure changes little after the halfway point in Fig. 16*(c)*. While the end state for the onset transient in Fig. 16*(f)* resembles the start state for the decay transient in Fig. 15*(a)*, the intermediate steps differ significantly. In particular, the instability onset case shows the entire center region of the combustor shifts in-phase over a very short time period, which is different from the decay process, where the flame shifts out-of-phase gradually, with the center region shifting first followed by the rest of the flame. The relative rapidity in which the combustor becomes in-phase for the onset transients is all the more surprising considering the longer timescale of the onset process. The onset transient also appears to settle into a number of intermediate amplitude limit cycles during the rise. An example occurs between Fig. 15*(c)* and Fig. 15*(d)*; the behavior

of these intermediary states is further supported by the quantized change in attractor diameter in the phase-space reconstruction videos of the transient provided in the supplemental materials. Fig. 16 indicates the intermediate amplitude limit cycles are *not* due to changes in the instantaneous phase relationships, as most of the center region is in-phase in Fig. 16*(c)* and Fig. 16*(d)*. This means the intermediate plateau amplitudes is caused by a decrease in the net combustor damping, which could be due to increased flame driving or decreased acoustic damping.

6.2. Long Duration Transients

Figure 17 shows $|\Phi(p') - \Phi(\dot{q}')|$ for a representative 10000 ms instability decay transient. The initial, unstable state shown in Fig. 17*a* resembles the initial unstable state for the short duration transient in Fig. 15*a*, as expected. Similarly, the end states for the long duration decay in Fig. 17*f* resembles the end state of the short duration decay in in Fig. 15*f*. While the beginning and end states of both long and short duration decay transients look similar, the growth of out-of-phase regions in the upper flame interaction region, visible in Fig. 15*c*, appear and disappear sporadically for the long transient decay. Figure 17*d* shows the appearance of an out-of-phase structure in the right center flame. These sporadic changes are more easily visualized in the videos of the transient decay included in the supplemental material.

Figure 18 shows $|\Phi(p') - \Phi(\dot{q}')|$ for a representative 10000 ms instability onset transient. The evolution of the long duration instability onset in Fig. 18 resembles the evolution of the short duration instability onset process in Fig. 16. The primary difference between the short and the long duration transient onset processes is the longer timescale for the long duration onset transient.

As shown in Fig. 18*b*, much of the center region of the combustor becomes in-phase with the pressure at the beginning of the transient, as indicated by the expansive dark region. This structure is maintained throughout the transient rise even when the pressure amplitude decreases, as in Fig. 16*c*.

7. Conclusions

This work examined the effects of fuel staging on stability transitions in a can combustor undergoing self-excited, longitudinal instability. Three staging amplitudes, five transient timescales, and two transient directions have been considered. Figure 5 shows that the staging amplitude must be above a minimum threshold, termed the "bifurcation equivalence ratio", in order to stabilize the combustor. The bifurcation equivalence ratio is found to be slightly greater than $\phi_{Staging} = 0.75$ and does not appear to depend on transient direction. The transient durations are divided into "short" duration transients, which are non-quasi-steady transients where $\tau_{Transient}$ is shorter than or on the order of τ determined from impulse transients, and "long" duration transients, which are quasi-steady transients that have $\tau_{Transient}$ greater than τ impulse. For short duration transients, we find the decay and onset timescales are largely independent of $\tau_{Transient}$. However, there is a strong directional dependence, where τ decay is significantly shorter and less variable than τ onset. The increased variability for τ onset is not likely due to valve performance, as τ_{Fuel} is not statistically significantly different for a given $\tau_{Transient}$. In contrast, instability transition timescales for long duration transients do depend on $\tau_{Transient}$ as would be expected. However, τ is significantly shorter than $\tau_{Transient}$, indicating the change in equivalence

ratio is quasi-steady-state relative to the stability transition.

The net combustor damping rates do not show a strong dependence on $\tau_{Transient}$ or direction. The staged-stable and unstable p'_{RMS} amplitudes are similarly insensitive to transient duration and direction. In all cases, when the combustor is unstable the center region is predominantly in-phase with constructive interference between heat release rates and pressure fluctuations. When the combustor is staged-stable, the instantaneous phase difference images show a the center of the combustor becomes predominantly out-of-phase. While the end states are independent of transient direction and duration at this operating condition, the evolution of the transition has a strong dependence on transient direction. For the instability decay transient, the center of the combustor goes out-of-phase first followed by the rest of the combustor. In contrast, for the instability onset transient, it is observed that the entire combustor goes in-phase at once even though the pressure increases over a longer timescale. We additionally find that short-duration transients evolve in a similar, less variable manner. In contrast, long-duration transients exhibit significant variability. This variability is attributed in part to the stepped change in pressure amplitudes during the long-duration transients, visible in the phase space reconstruction shown in the supplemental material. This stepped variation implies that the combustor damping rate also changes in a stepwise fashion during long duration transients, which differs from the more rapid and continuous change observed for the short duration transients. Future work will use OH planar laser induced fluorescence to examine the flame edge dynamics of the staged flame to better explain the trends observed in this work.

8. Acknowledgments

The authors thank Dr. Bryan Quay at Penn State and Dr. Keith McManus at GE Global Research for their helpful suggestions and insights on the project. The authors also thank the United States Department of Energy for funding this work under award number DE-FE0025495 and contract monitor Mark Freeman.

9. References

[1] T. C. Lieuwen, V. Yang, Combustion Instabilites in Gas Turbine Engines, Vol. 210 of Progress in Astronautics and Aeronautics, American Institute of Aeronautics and Astronautics, 2005.

[2] T. C. Lieuwen, V. Yang, Gas Turbine Emissions, Vol. 38, Cambridge University Press, 2013.

[3] J. Hermann, A. Orthmann, S. Hoffmann, P. Berenbrink, Combination of active instability control and passive measures to prevent combustion instabilities in a 260mw heavy duty gas turbine, RTO AVT Symposium, 2000.

[4] T. Poinsot, B. Yip, D. Veynante, A. Trouv, J. Samaniego, S. Candel, Active control: an investigation method for combustion instabilities, Journal de physique III 2 (7) (1992) 1331–1357.

[5] G. Bulat, D. Skipper, R. McMillan, K. Syed, Active control of fuel splits in gas turbine dle combustion systems, in: ASME Turbo Expo 2007: Power for Land, Sea, and Air, no. GT2007-27266, 2007.

[6] J. Cohen, G. Hagen, A. Banaszuk, S. Becz, P. Mehta, Attenuation of combustor pressure oscillations using symmetry breaking, AIAA Paper No. GT2011-0060.

[7] J. Samarasinghe, W. Culler, B. D. Quay, D. A. Santavicca, J. O'Connor, The effect of fuel staging on the structure and instability characteristics of swirl-stabilized flames in a lean premixed multi-nozzle can combustor.

[8] L. Li, X. Sun, C. Lioi, V. Yang, Effect of azimuthally nonuniform heat release on longitudinal combustion instabilities, Journal of Propulsion and Power 33 (1) (2016) 193–203.
URL http://dx.doi.org/10.2514/1.B36055

[9] P. Denholm, M. O'Connel, G. Brinkman, J. Jorgenson, Overgeneration from solar energy in California: A field guide to the duck chart, Report, National Renewable Energy Laboratory (2015).

[10] K. T. Kim, S. Hochgreb, Measurements of triggering and transient growth in a model lean-premixed gas turbine combustor, Combustion and Flame 159 (3) (2012) 1215–1227.

[11] L. Kabiraj, R. I. Sujith, P. Wahi, Bifurcations of self-excited ducted laminar premixed flames, Journal of Engineering for Gas Turbines and Power 134 (3) (2011) 031502–031502.
URL http://dx.doi.org/10.1115/1.4004402

[12] H. Gotoda, H. Nikimoto, T. Miyano, S. Tachibana, Dynamic properties of combustion instability in a lean premixed gas-turbine combustor, Chaos: An Interdisciplinary Journal of Nonlinear Science 21 (1) (2011) 013124.
URL http://dx.doi.org/10.1063/1.3563577

[13] M. R. Bothien, J. P. Moeck, C. O. Paschereit, Comparison of linear stability analysis with experiments by actively tuning the acoustic boundary conditions of a premixed combustor, Journal of Engineering for Gas

Turbines and Power 132 (12) (2010) 121502–121502.
URL http://dx.doi.org/10.1115/1.4000806

[14] N. Noiray, A. Denisov, A method to identify thermoacoustic growth rates in combustion chambers from dynamic pressure time series, Proceedings of the Combustion Institute 36 (3) (2017) 3843–3850.

[15] S. Kheirkhah, B. Geraedts, P. Saini, K. Venkatesan, A. Steinberg, Non-stationary local thermoacoustic phase relationships in a gas turbine combustor, Proceedings of the Combustion Institute 36 (3) (2017) 3873–3880.

[16] I. Boxx, C. D. Carter, K.-P. Geigle, W. Meier, B.-A. Kumgeh, J. Lewalle, A study of spontaneous transition in swirl-stabilized flames, in: ASME Turbo Expo 2017, Charlotte, North Carolina, ASME, ASME, 2017.

[17] V. Nair, R. I. Sujith, Intermittency as a transition state in combustor dynamics: An explanation for flame dynamics near lean blowout, Combustion Science and Technology 187 (11) (2015) 1821–1835.
URL http://dx.doi.org/10.1080/00102202.2015.1066339

[18] B. D. Bellows, Y. Neumeier, T. Lieuwen, Forced response of a swirling, premixed flame to flow disturbances, Journal of propulsion and power 22 (5) (2006) 1075–1084.

[19] B.-J. Lee, J. Lee, D. Santavicca, Detection of the onset of unstable combustion in lean premixed combustors, in: 42 nd AIAA Aerospace Sciences Meeting and Exhibit.

[20] I. Boxx, K.-P. Geigle, C. D. Carter, J. Lewalle, B.-A. Kumgeh, Non-stationary local thermoacoustic phase relationships in a gas turbine combustor, in: 55th AIAA Aerospace Sciences Meeting, Grapevine, Texas, AIAA, AIAA, 2017.

[21] J. Samarasinghe, S. J. Peluso, B. D. Quay, D. A. Santavicca, The three-dimensional structure of swirl-stabilized flames in a lean premixed multi-nozzle can combustor, Journal of Engineering for Gas Turbines and Power 138 (3) (2015) 031502.
URL http://dx.doi.org/10.1115/1.4031439

[22] P. Orawannukul, An experimental study of forced flame response in technically premixed flames in a lean premixed gas turbine combustor, Thesis, The Pennsylvania State University (2014).

[23] J. G. Lee, D. A. Santavicca, Experimental diagnostics for the study of combustion instabilities in lean premixed combustors, Journal of Propulsion and Power 19 (5) (2003) 735–750.
URL http://dx.doi.org/10.2514/2.6191

[24] V. Nori, J. Seitzman, Evaluation of chemiluminescence as a combustion diagnostic under varying operating conditions, AIAA paper 953.

[25] T. C. Lieuwen, Experimental investigation of limit-cycle oscillations in an unstable gas turbine combustor, Journal of Propulsion and Power 18 (1) (2002) 61–67.
URL http://dx.doi.org/10.2514/2.5898

[26] N. V. Stadlmair, T. Hummel, T. Sattelmayer, Thermoacoustic damping rate determination from combustion noise using bayesian statistics

[27] T. Lieuwen, Online combustor stability margin assessment using dynamic pressure data, Journal of engineering for gas turbines and power 127 (3) (2005) 478–482.

[28] D. Mejia, M. Miguel-Brebion, L. Selle, On the experimental determination of growth and damping rates for combustion instabilities, Combustion and Flame 169 (2016) 287–296.

[29] F. Culick, P. Kuentzmann, Unsteady motions in combustion chambers for propulsion systems, Tech. rep., NATO Research and Technology Organization Neuilly-Sur-Seine (2006).

[30] M. Plummer, JAGS Version 4.0.0 User Manual (2015).

[31] N. Noiray, Linear growth rate estimation from dynamics and statistics of acoustic signal envelope in turbulent combustors, Journal of Engineering for Gas Turbines and Power 139 (4) (2017) 041503.

[32] R. McGill, J. W. Tukey, W. A. Larsen, Variations of box plots, The American Statistician 32 (1) (1978) 12–16.

[33] R. R. Wilcox, Introduction to robust estimation and hypothesis testing, Academic press, 2011.

[34] W. Culler, X. Chen, S. Peluso, D. A. Santavicca, J. O'Connor, Comparison of center nozzle staging to outer nozzle staging in a multi-flame combustor, in: ASME Turbo Expo 2018, Oslo, Norway, ASME, 2018.

[35] J. Samarasinghe, S. Peluso, M. Szedlmayer, A. De Rosa, B. Quay, D. Santavicca, Three-dimensional chemiluminescence imaging of unforced and forced swirl-stabilized flames in a lean premixed multi-nozzle can combustor, Journal of Engineering for Gas Turbines and Power 135 (10) (2013) 101503.
URL http://dx.doi.org/10.1115/1.4024987

List of Figures

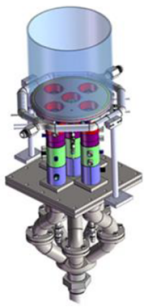

Figure 1: Multinozzle Combustor

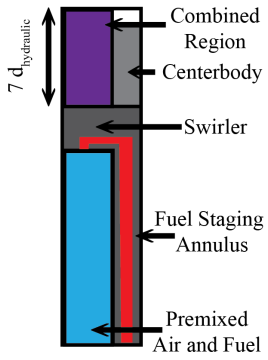

Figure 2: Staging Fuel Flow Path

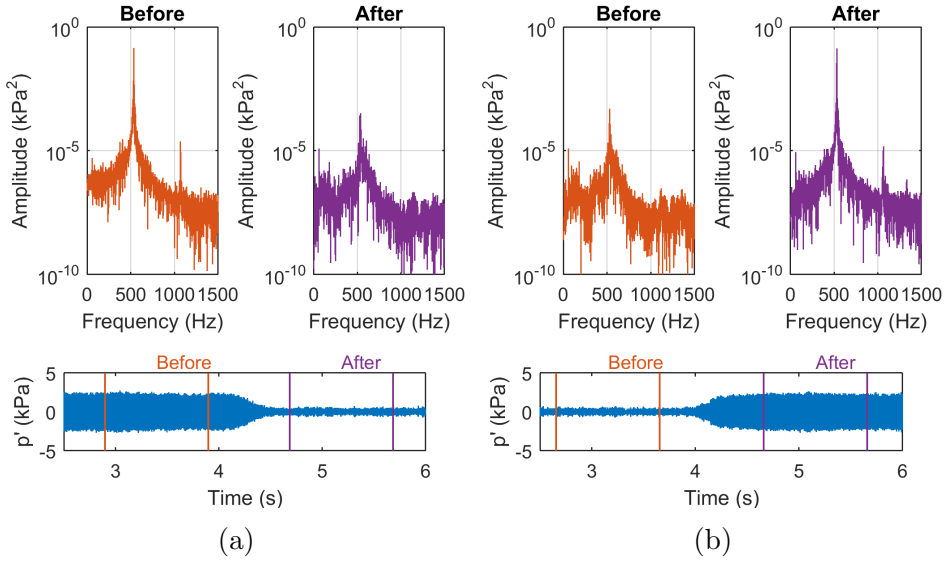

Figure 3: Pressure Time Trace and Power Spectral Density for (a) Decay Transient and (b) Onset Transient

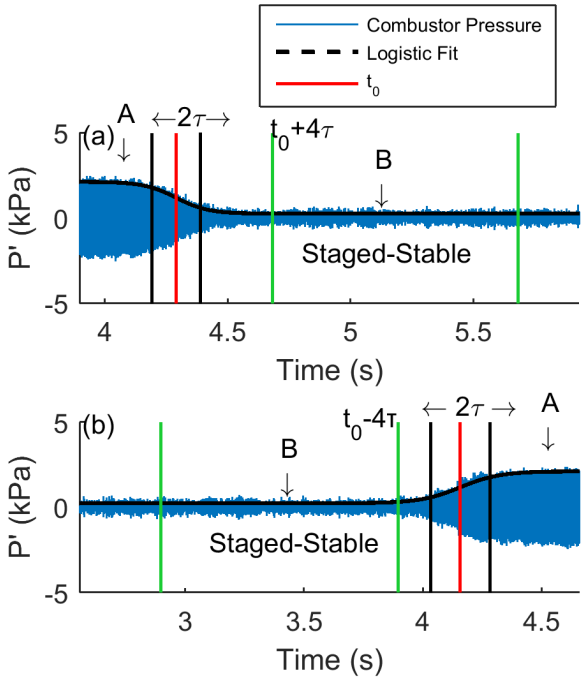

Figure 4: Illustration of Logistic Fit applied to (a) Instability Decay Transition and (b) Instability Onset Transition

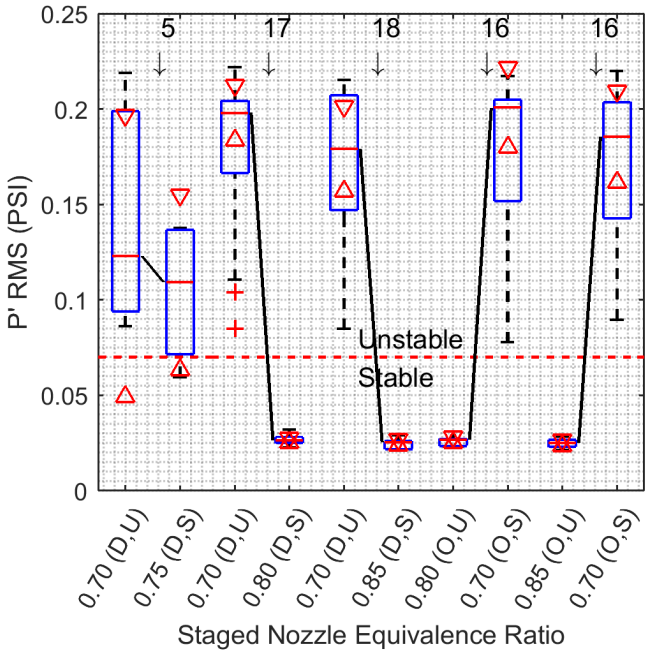

Figure 5: Boxplots of p'_{RMS} before and after impulse transients

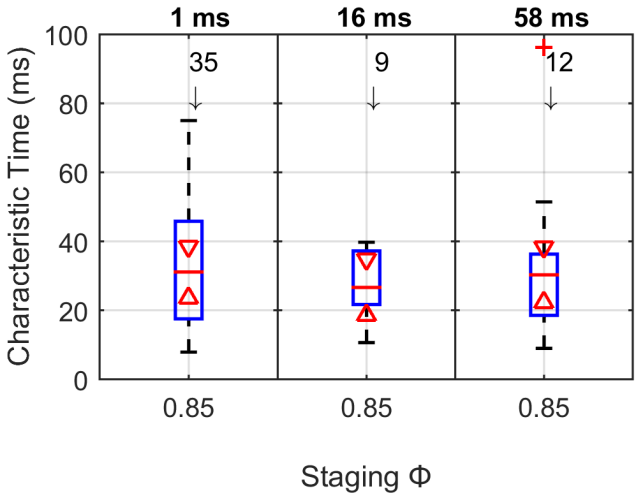

Figure 6: Boxplots of characteristic decay times for short transients. The valve timescale is shown by the title of each subplot and the total number of ensembles at each condition given by the number above the arrow.

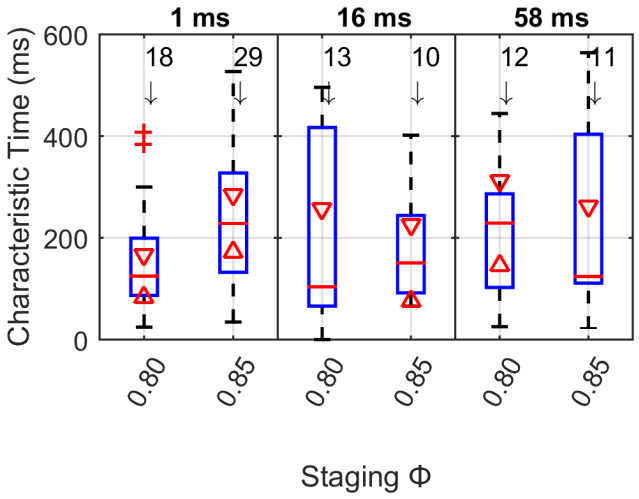

Figure 7: Boxplots of characteristic rise times for short transients. The valve timescale is shown by the title of each subplot and the total number of ensembles at each condition given by the number above the arrow.

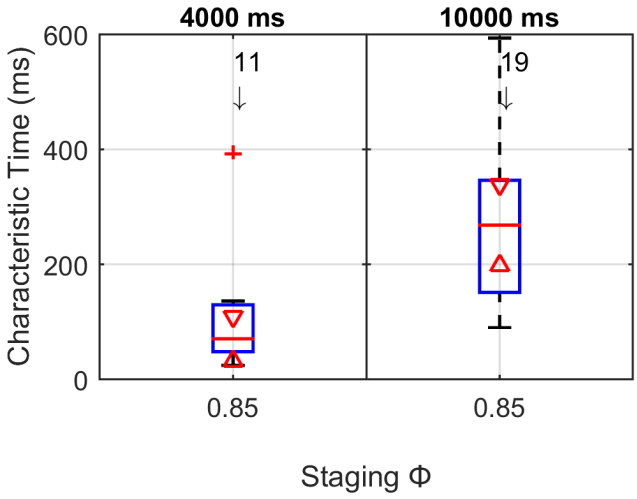

Figure 8: Boxplots of characteristic decay times for long transients. The valve timescale is shown by the title of each subplot and the total number of ensembles at each condition given by the number above the arrow.

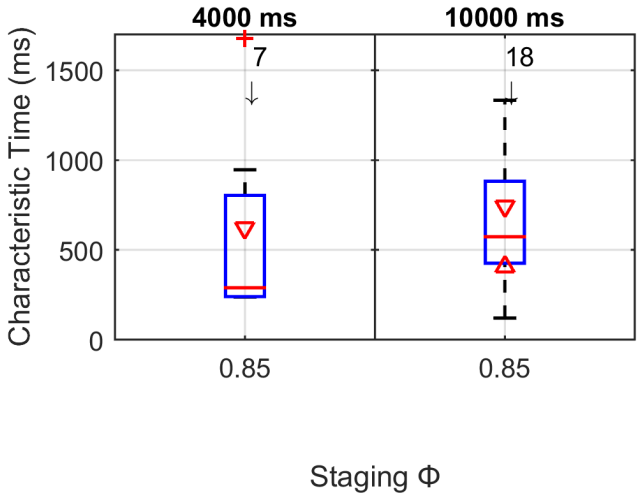

Figure 9: Boxplots of characteristic rise times for long transients. The valve timescale is shown by the title of each subplot and the total number of ensembles at each condition given by the number above the arrow.

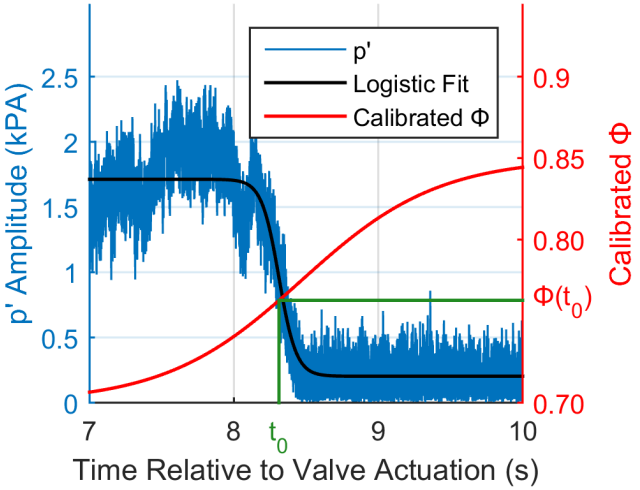

Figure 10: Illustration of Bifurcation Equivalence Ratio

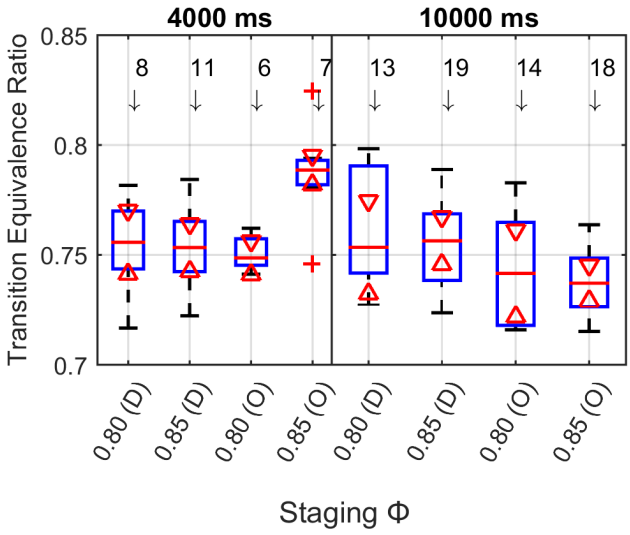

Figure 11: Bifurcation Equivalence Ratios for Long Duration Transients

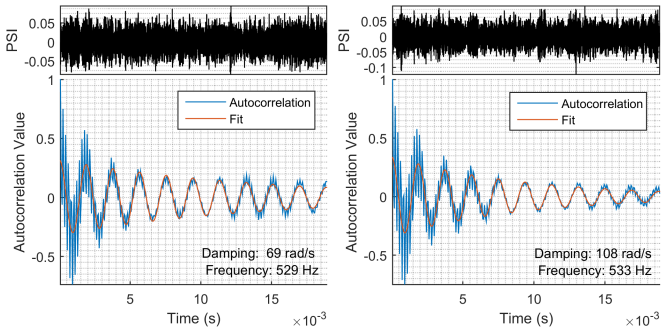

(a) (b)

Figure 12: Measured Damping for Median Impulse Decay Transients for *(a)* $\phi_{Staging} = 0.80$ and *(b)* $\phi_{Staging} = 0.85$

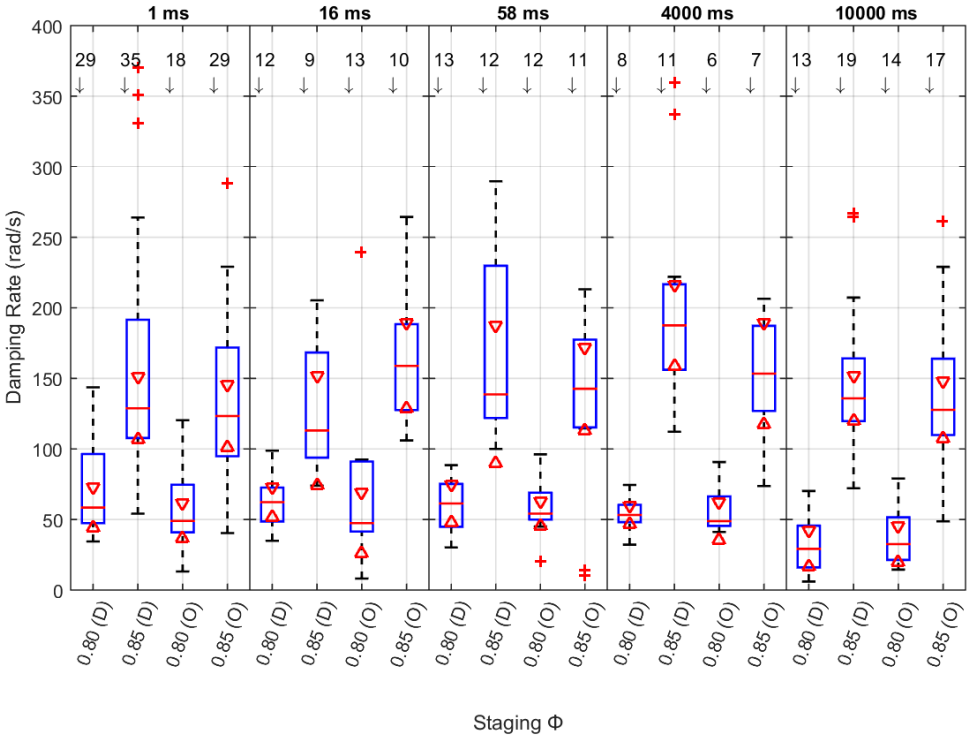

Figure 13: Boxplots of Combustor Damping Rates

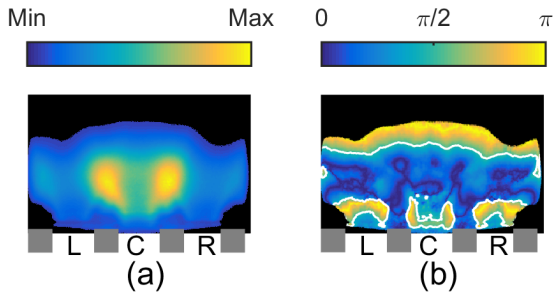

Figure 14: Comparison of Time-Averaged CH* Chemiluminescence (a) and Instantaneous Phase Images (b)

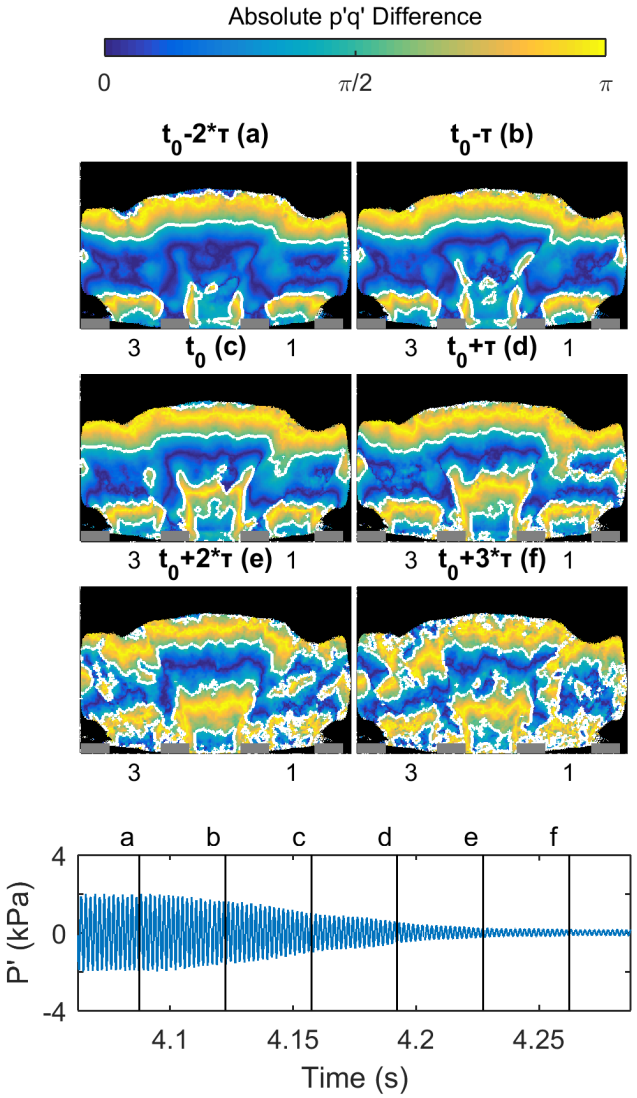

Figure 15: Instantaneous, Absolute Phase Difference between p' and $\dot{q}'$ for median $\phi_{Staging} = 0.85$ 1 ms Decay Transient. Video of the transient is in Figure 15 Supplemental Material online.

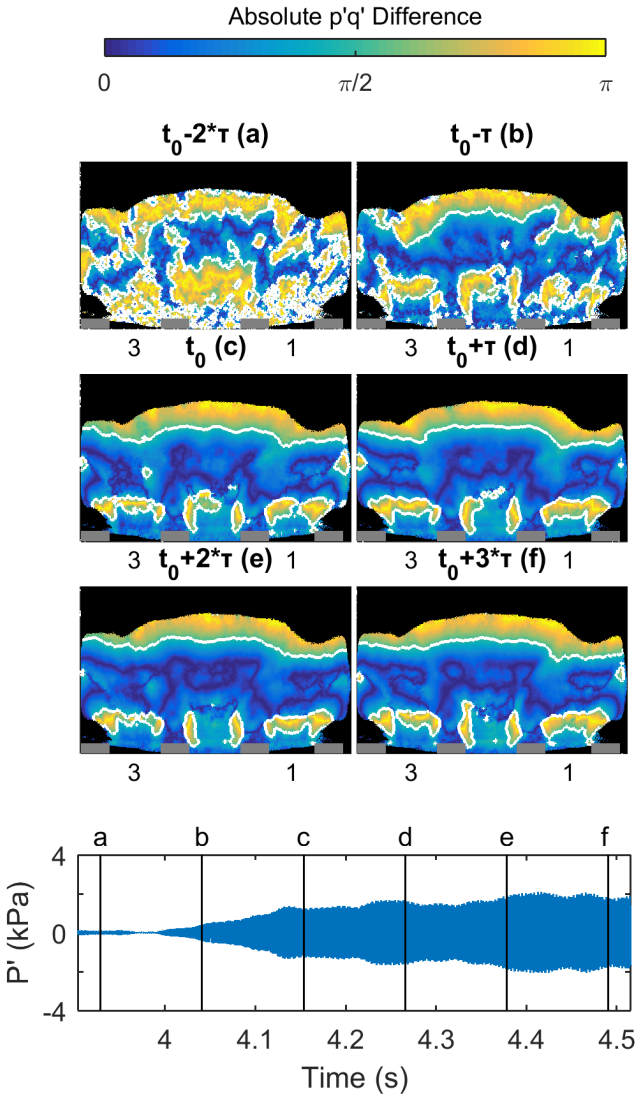

Figure 16: Instantaneous, Absolute Phase Difference between p' and $\dot{q}'$ for $\phi_{Staging} = 0.85$ 1 ms Onset Transient. Video of the transient is in Figure 16 Supplemental Material online.

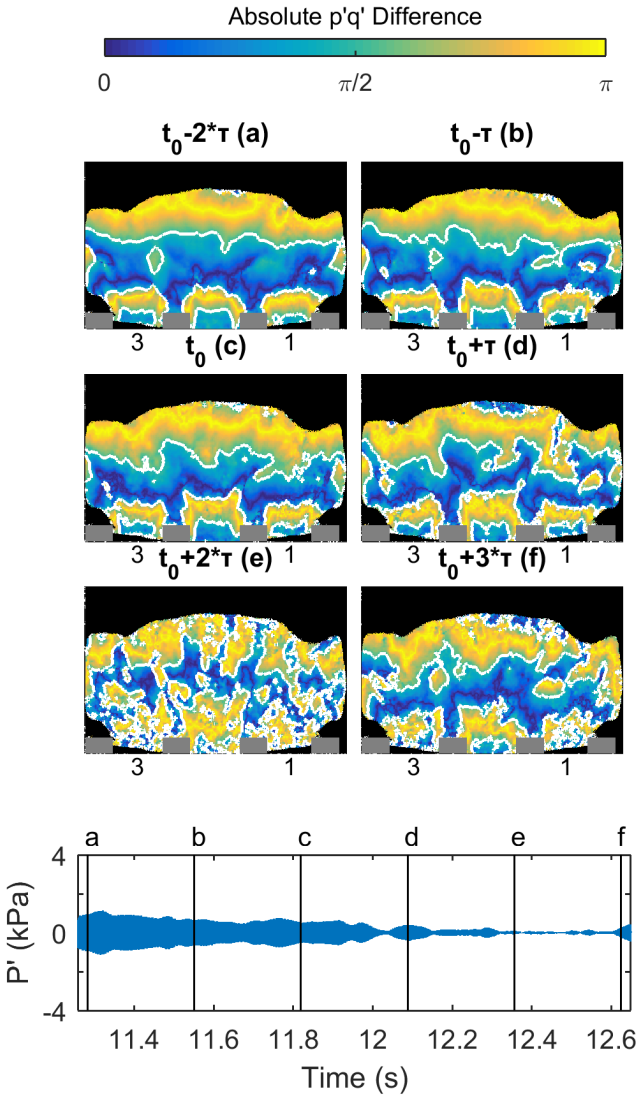

Figure 17: Instantaneous, Absolute Phase Difference between p' and $\dot{q}'$ for $\phi_{Staging} = 0.85$ 10000 ms Decay Transient. Transient. Video of the transient is in Figure 17 Supplemental Material online.

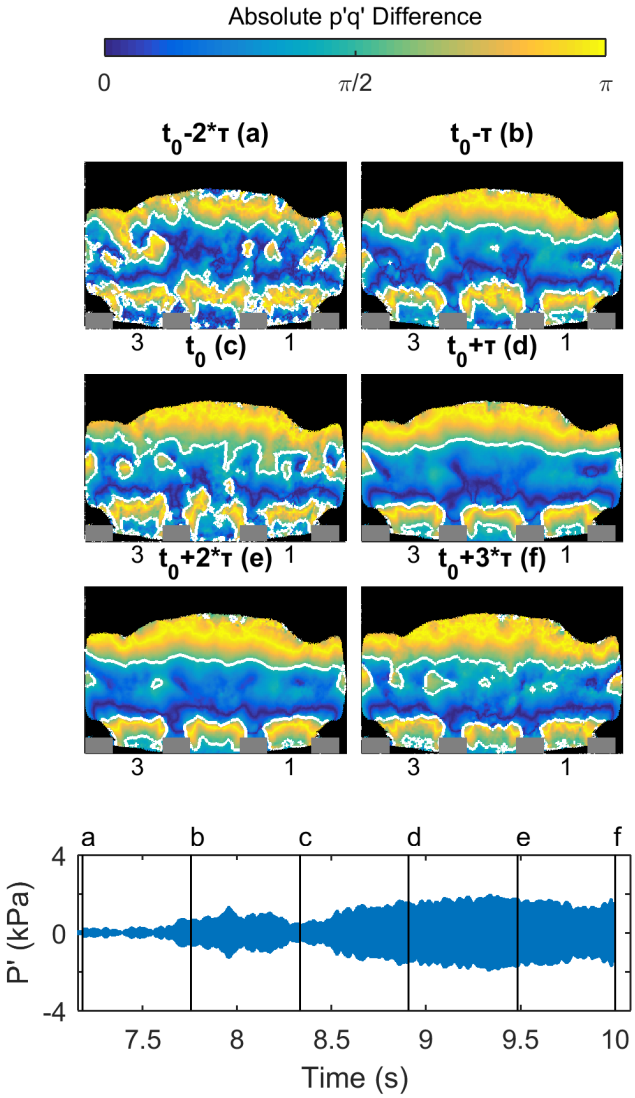

Figure 18: Instantaneous, Absolute Phase Difference between p' and $\dot{q}'$ for $\phi_{Staging} = 0.85$ 10000 ms Onset Transient. Transient. Video of the transient is in Figure 18 Supplemental Material online.